RESEARCH ARTICLE

Temperature-mediated tribological characteristics of 40CrNiMoA steel and Inconel 718 alloy during sliding against Si₃N₄ counterparts

Liuyang BAI[1,2], **Shanhong WAN**[1,2,*], **Gewen YI**[1,2,*], **Yu SHAN**[1], **Sang The PHAM**[3], **Anh Kiet TIEU**[3], **Yan LI**[4], **Rendong WANG**[5]

[1] *State Key Laboratory of Solid Lubrication, Lanzhou Institute of Chemical Physics, Chinese Academy of Sciences, Lanzhou 730000, China*

[2] *Center of Materials Science and Opto-Electronics Engineering, University of Chinese Academy of Sciences, Beijing 100049, China*

[3] *Faculty of Engineering and Information Sciences, University of Wollongong, Wollongong 2522, Australia*

[4] *State Key Laboratory of Metal Materials for Marine Equipment and Application, Anshan 114009, China*

[5] *Ansteel Iron & Steel Research Institute, Anshan 114009, China*

© The author(s) 2020.

Abstract: A comparative evaluation of the friction and wear behaviors of 40CrNiMoA steel and Inconel 718 alloy sliding against Si₃N₄ counterparts was conducted over a large temperature range from room temperature (RT) to 800 ℃. The temperature-dependent tribological properties associated with the resulting chemical mitigation and structural adaptation of the solid sliding surface were clarified by surface/interface characterizations. The results revealed desirable performance in reducing friction and wear at elevated temperatures, which was associated with the resulting oxide composite film's adaptive lubricating capability, whereas severe abrasive wear occurred at room/ambient temperatures. The oxidative-abrasive differentials for the two alloys were further discussed by considering the combined effect of temperature and stressed-shearing conditions.

Keywords: steel alloys; high-temperature tribology; wear and friction; oxidation; surface/interface chemistry

1 Introduction

High-temperature tribological characteristics of high-strength alloyed materials have been studied considerably in aerospace, power generation, material processing, and metalworking industries. A series of problems occur simultaneously between frictional contacts, such as abrasion, plastic deformation, and fatigue [1]. During high-temperature friction, oxides preferentially form on the worn surface [2], and their thicknesses play a pivotal role in tribological performance [3]. If the tribochemically grown oxide layer behaves effectively, it can deliver the desired lubricity between the rubbing contacts at elevated temperatures [4]. However, not all *in situ* grown oxide layers perform favorably. Temperature has a significant effect on tribological varieties of alloyed materials [5, 6]. Thus, attempts to comprehend the tribological capabilities and underlying mechanism of alloyed materials in terms of microstructure transition and composition migration across the sliding surface/interface are still ongoing.

At room/ambient temperatures, the frictional

---

surface suffers dominant abrasion [1, 7]. Because the operational temperature is not sufficiently high to grind the wear debris and thus a continuous protection layer is not present, the abrasion and subsequent oxidation interact with each other, thereby leading to severe wear and unexpected abrading of the three body [8]. The applied force and total sliding distance are the predominant factors in the wear process, during which the kinetics of oxidation at the sliding surface, other than temperature, contribute significantly to the acceleration of wear.

A severe-to-moderate wear transition emerges between the rubbing contact as the temperature exceeds a critical temperature, which is attributed to a compliant oxide layer [9]. This oxide layer is often termed "glaze", which evolves from the oxide debris by the tribo-sintering process. This layer also displays a composite feature consisting amorphous and nanocrystalline components. Such structural assembly enables accommodation of the interfacial stresses [10], which is considered to be the major plasticity activator that renders desirable ductility when exposed to harsh temperatures. However, the tribological capability of this oxide layer is further associated with the reduction of the mechanical strengths of materials at elevated temperatures [11], variations in surface conditions and adhesion due to oxidation and diffusion [12], phase change, and composition change [13], which inherently depends on the temperature.

Both 40CrNiMoA steel and Inconel 718 alloy have superior strengths and toughnesses for equipment manufacturing and aerospace industries [14, 15]. They have been widely applied as high-temperature substrates for coating deposition. However, the capabilities to withstand friction and wear of the two alloys themselves have not been comprehensively investigated for a wide range of temperatures. In particular, knowledge of the tribological discrepancy between nickel-based (Inconel 718 alloy) and iron-based (40CrNiMoA steel) alloys at elevated temperatures is still a little far from the industrial demand in machinery components, which often require working in harsh temperature conditions. In this study, the tribological dependencies of these two alloyed materials are investigated comparatively during sliding against a ceramic Si_3N_4 counterpart at different temperatures. In addition to the connection between temperature and the resulting tribological properties, the surfaces and interface of the worn 40CrNiMoA steel and Inconel 718 alloy are analyzed in terms of the resulting oxide layer to clarify the wearing mechanism and frictional evolution. The findings of this study will be potentially instructive for the manufacturing of high-strength alloys and the availability of ceramic silicon nitride as a manufacturing tool in harsh hot air environments.

2   Experimental

2.1   Applied materials

Two different alloys were investigated in this study: 40CrNiMoA steel and Inconel 718 alloy. Commercial 40CrNiMoA steel (AISI 4340) was purchased from Jiangyin Xingcheng Special Steel Works Co. Ltd., while the superalloy Inconel 718 was purchased from Suzhou Feiyue Precision Machinery Co. Ltd. Table 1 shows the chemical composition of 40CrNiMoA steel and Inconel 718 superalloy. Predominantly Fe, along with all other alloying elements, make up 40CrNiMoA high-strength steel, while the three main components of Ni, Fe, and Cr are included within the as-received Inconel 718 alloy.

Table 1   Chemical compositions of 40CrNiMoA steel and Inconel 718 superalloy (wt%).

	C	O	Mo	Al	Nb	Mn	Ti	Cr	Fe	Ni
40CrNiMoA	2.53	0.77	0.05	—	—	0.37	—	0.45	95.12	0.71
Inconel 718	2.31	0.62	1.25	0.29	2.15	—	0.51	17.28	15.58	60.01

Note: – indicates that it is not detected.

Figure 1 displays the metallurgical phase of the two alloyed materials with the assistance of the spot energy-dispersive spectroscopy (EDS). 40CrNiMoA steel consists of tempered martensite, retained austenite, and some precipitated granular carbides (spot 1 in Fig. 1(b) and Fig. 1(c)). It is identifiable that ultra-fine carbides are distributed homogeneously within the lath-shaped martensite matrix. As shown in Fig. 1(d) and spot 4 in Fig. 1(e), Inconel 718 alloy demonstrates a net-like convex structure

with a dominant carbide (Nb and Mo) composition along the grain boundary [16] within the austenitic matrix, while such needle-like δ phases are invisible. In addition, the γ'' (Ni_3Nb) precipitate can be distinguished [17] according to the EDS in Fig. 1(f) because of the chemical affinities of Ni and Nb.

Disk specimens for the friction and wear testing had dimensions of Φ24 mm × 8 mm, which were cut from 40CrNiMoA steel and Inconel 718 alloy
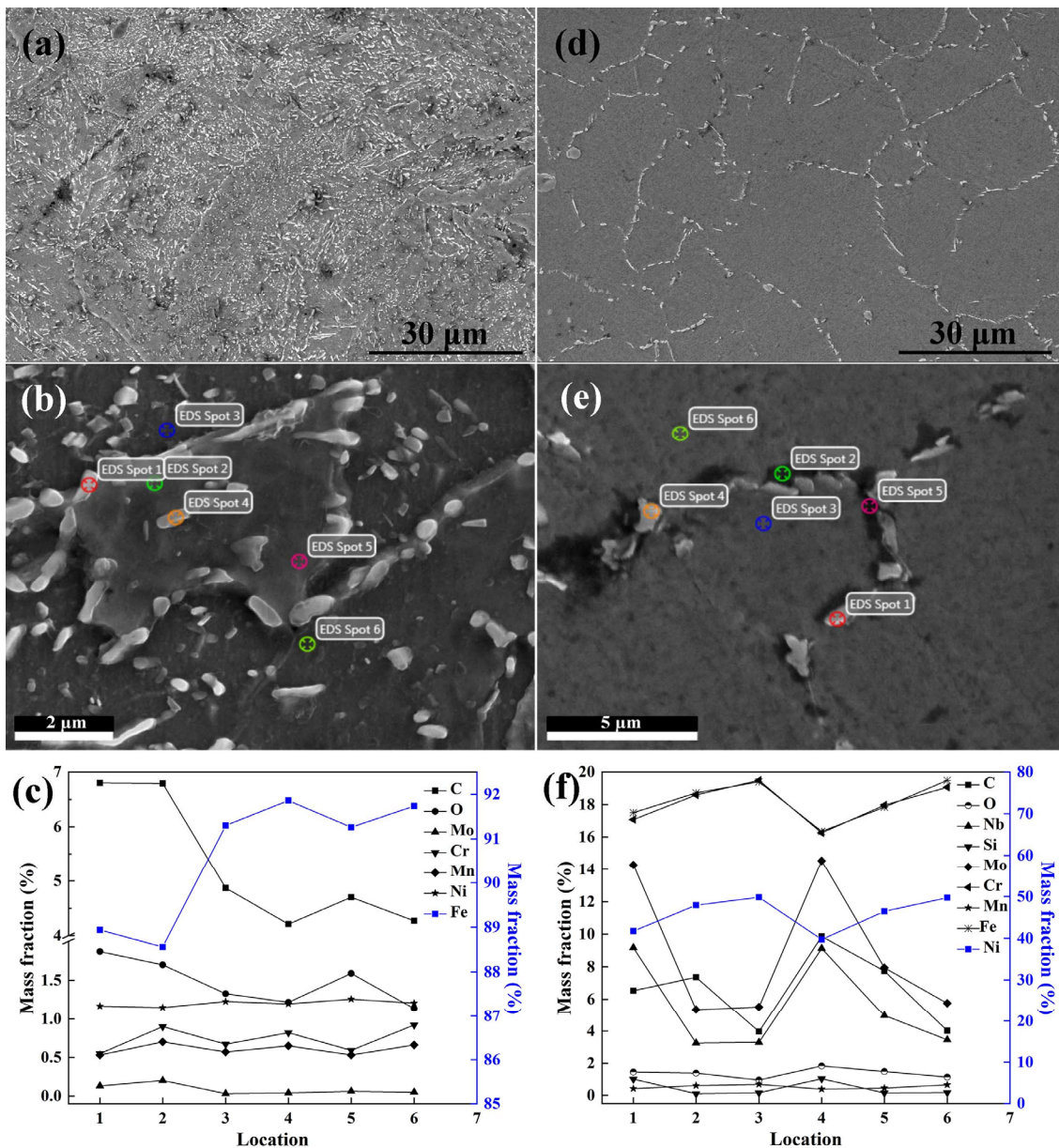

Fig. 1 Microstructure and metallurgical composition analyses of the alloyed materials. (a–c) 40CrNiMoA steel, and (d–f) Inconel 718 alloy.

bars. All the disk specimens were machined to a surface roughness, Ra, of approximately 0.02 μm. Because Si_3N_4 has excellent mechanical strength and high thermal stability without any deformation at 800 ℃ [18], Si_3N_4 (Φ 6 mm, Ra 0.02 μm) was selected as the counterpart material for this work and was purchased from Shanghai Unite Technology Co. Ltd. The Si_3N_4 ball had a chemical composition (wt%) consisting of N 41.27%, O 19.57%, Al 2.17%, Y 1.57%, Nb 13.5%, Ti 0.22%, and Si in balance. Prior to tribological testing, the disk and ball were ultrasonically cleaned for 15 min in a solution of acetone, and then dried in hot air.

2.2 Mechanical and tribological evaluation

The microhardness of the two alloys was measured using an MH-5-VM microhardness tester, which was manufactured by Shanghai Hengyi Science and Technology Co. Ltd., with a Vickers pyramid-shaped diamond indenter with an angle of 136° between opposite faces. At least 11 microhardness values were taken from each sample under different loadings, with a dwell time of 5 s. Scratch tests were carried out using an RST^3 scratch machine (Anton Paar, Switzerland) using a conical diamond indenter with a radius of 200 μm and cone angle of 120°. Scratch testing was performed with a linearly increasing load from 0 to 50 N at a normal loading speed of 98 N/min and a scratch length of 5 mm.

The tribological performances of 40CrNiMoA steel and Inconel 718 alloy sliding against Si_3N_4 were tested using a high-temperature ball-on-disk tribometer (UMT-3, Bruker Corp, USA) in air with a relative humidity of 20%±5% at 25 ℃. The upper specimen was a Si_3N_4 ball, while the bottom disk specimen was composed of 40CrNiMoA steel or Inconel 718 alloy. All rotation tests were carried out at a sliding speed of 0.104 m/s (200 rotations/min), an applied load of 10 N, a wear track radius of 5 mm, and a duration of 1 h. The testing temperatures were room temperature (RT, 25 ℃), 200, 400, 600, and 800 ℃. Before the frictional test started, the tribosystem was heated up to the target temperature with a heating rate of 10 ℃/min. In order to ensure the reproducibility of the data,

each frictional test was repeated at least twice.

The friction coefficient of the specimen was automatically recorded by a computer attached to the UMT-3, and the wear rate, in $mm^3/(N·m)$, was calculated according to Eq. (1),

$$\omega = \Delta V / (F \cdot S) \tag{1}$$

where ΔV is the wear volume loss in mm^3, S is the sliding distance in m, and F is the load in N. The volume loss ΔV_1 of the sample was acquired by Eq. (2),

$$\Delta V_1 = 2\pi R S \tag{2}$$

where R is the wear radius of the sample, and S is the cross-sectional area of the wear track. The wear volume ΔV_2 of the counterpart was obtained by a geometric method of measuring the wear scar diameter of the ball with a confocal laser scanning microscope (Olympus BX53, Japan). ΔV_2 was calculated according to Eq. (3) [19]:

$$\Delta V_2 = \frac{\pi}{12}\left(R - \sqrt{R^2 - \frac{D^2}{4}} \right)\left(D^2 + 4R^2 - 4R\sqrt{R^2 - \frac{D^2}{4}} \right) \tag{3}$$

where R is the radius of the ball and D is the diameter of the worn scar.

2.3 Characterization

The surface roughness values of all disk specimens were measured using a type 2206 surface roughness instrument manufactured by Harbin Measuring Cutting Tool Group Co. Ltd. A surface profiler (KLA Tencor D-100, USA) was used to evaluate the wear loss by scanning the wear track on the disk. The metallurgical identification between 40CrNiMoA steel and Inconel 718 alloy was performed by field emission scanning electron microscopy (FESEM; FEI Apreo S, USA). The quantitative analyses of the elements were performed by EDS with backscattered electron imaging (BSE) at 20 kV. Prior to the metallurgical analysis, 40CrNiMoA steel was etched with nital for 50 s (4% HNO_3 in alcohol solution), and the Inconel 718 alloy was etched with a special reagent (5 g $CuCl_2$, 100 mL HCl, and 100 mL anhydrous alcohol). The damaged surfaces and interface at the central zone of the wear track were further analyzed by scanning electron microscopy (SEM)/EDS, where the thickness of the tribolayer could be determined from the cross-sectional-view image. Using BSE imaging, light elements were

depicted as darker than heavy elements; for example, the iron-based material appears lighter, and the abrasive particles of oxide appear darker [20]. The representative compositions of worn and unworn surfaces were analyzed using a Raman spectrometer (LabRAM HR Evolution, HORIBA Jobin Yvon S.A.S. France) with a solid-state laser having an excitation wavelength of 532 nm in a window from 100 to 1,800 cm^{-1}. The Raman data were collected continuously using a 30 s exposure time with two accumulations.

3 Results and discussion

3.1 Mechanical evaluation of the two alloys

The average microhardness values of 40CrNiMoA steel and Inconel 718 alloy are given in Table 2. Because the dominant γ'(Ni$_3$Nb) and γ'(Ni$_3$(Al, Ti)) phases, along with other alloying elements such as Nb, Al, and Ti, render a superior strengthening effect, Inconel 718 alloy has a hardness twice as

Table 2 Vickers hardness of the two alloys under different loadings.

Samples	Load (g)		
	50	100	200
40CrNiMoA	240.0±12.1 HV	233.4±16.5 HV	221.6±10.9 HV
Inconel 718	483.8±9.8 HV	480.0±10.6 HV	471.8±8.3 HV

high as that of 40CrNiMoA steel. As the applied loading increases, the indentation size becomes larger, and the microhardness values decrease gradually. This phenomenon is known as the indentation size effect (ISE) [21, 22].

A qualitative comparison was further performed by checking the deformed cavity [23], as shown in Fig. 2. Even though the applied loading increases to 200 g, such characteristic radial cracks cannot be observed, which reflects the high mechanical toughness values and considerable ductilities of both alloys. However, there is a clearly visible deformation at the edge of the 40CrNiMoA steel specimen after indentation due to plastic
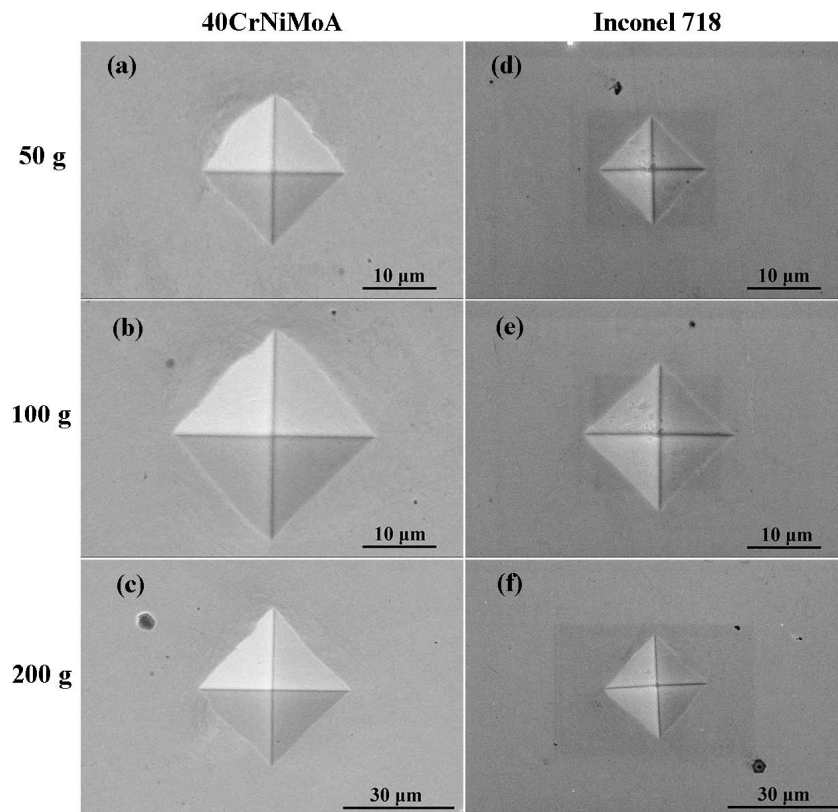

Fig. 2 SEM micrographs of microhardness indentation of (a–c) 40CrNiMoA steel, and (d–f) Inconel 718 alloy under applied loadings of 50, 100, and 200 g.

anisotropy [24, 25], which can be seen in Fig. 2(c). On the contrary, Inconel 718 alloy does not demonstrate any mechanically induced damage, as shown in Figs. 2(d)–2(f). These microscopic observations prove that Inconel 718 alloy has a better mechanical capability than 40CrNiMoA steel.

Figure 3 shows the scratch features of 40CrNiMoA steel and Inconel 718 alloy after one-pass scratch testing, where the scratching depth values at different locations are automatically recorded by the RST3 scratch machine. The penetration depth and maximum residual depth of 40CrNiMoA steel are 23 and 18.5 μm, respectively, while Inconel 718 alloy has a penetration depth of 20.8 μm and a maximum residual depth of 6.2 μm. As compared with the scratch track of Inconel 718 alloy, noticeable increases in scratch depth and width occur for the 40CrNiMoA steel with increasing applied loading. It was elucidated that severe delamination occurs for 40CrNiMoA steel, and Inconel 718 alloy demonstrates better resistance to scratching due to its superior strength [26].

Relevant failing mechanisms were further observed in Fig. 4. Under the continuous abrasion process with coupled vertical and lateral forces, 40CrNiMoA steel displays severe plastic deformation with the characteristics of the plowing action depicted in Figs. 4(a) and 4(c), where materials are squeezed out to both sides and visible bulges emerge along the scratch tracks. At a higher level of loading, the cracks are inclined to tear, and micro-cracking accompanied by a mild cutting mechanism takes place, yielding the highest scratch depth in Fig. 4(e). Similar failures, that is, the crack formed by tensile frictional stress

behind the trailing edge of the stylus, can be found during the scratching evaluation of the coating material [27]. Inconel 718 alloy displays a mildly similar evolution as the scratching load increases, as shown in Fig. 4(b); however, a smoothening track without any cracks and craters appears. The failure mechanism is the plowing process, which is strongly associated with the good combination of ductility and strength of the Inconel 718 alloy [28]. In particular, the γ phase of the Inconel 718 alloy matrix has a face-centered cubic structure with 12 independent slip systems, and it deforms plastically in a slipping form, as evidenced by the slip bands in Fig. 4(d). Based on these comprehensive mechanical evaluations, Inconel 718 alloy yields abrasion resistance and mechanical strength superior to those of 40CrNiMoA steel.

3.2 High temperature friction and wear

The averaged coefficients of friction (COF) of 40CrNiMoA steel and Inconel 718 alloy against the Si_3N_4 counterpart are summarized in Fig. 5. Their frictional behaviors at different operational temperatures display some similarities for the two tribological pairs, temperature dependent. The COF of 40CrNiMoA steel and Inconel 718 alloy decreases with increasing operational temperatures. The COF at RT is 0.88 for 40CrNiMoA steel and 0.78 for Inconel 718 alloy, respectively. The results from tests at 800 ℃ illustrate that the COFs of 40CrNiMoA steel and Inconel 718 alloy reach the minimum values, which are as low as 0.52 and 0.32, respectively. In total, the COF of 40CrNiMoA steel is relatively higher than that of Inconel 718 alloy for a wide range of testing temperatures. It can be
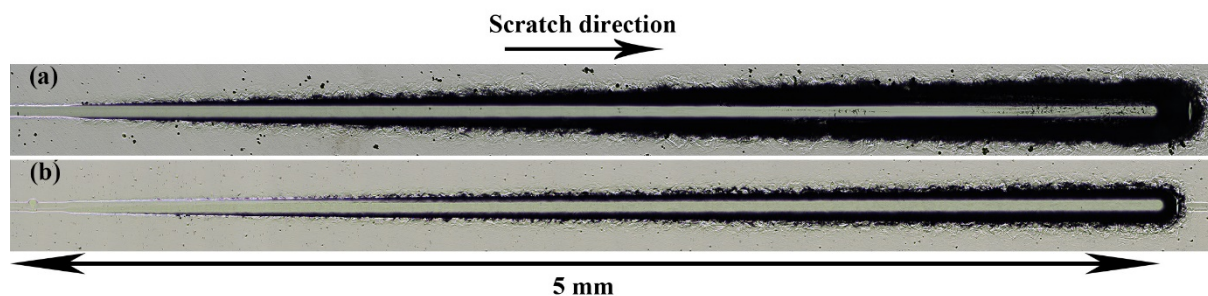

Scratch direction

5 mm

Fig. 3 Optical observation of scratch tracks of (a) 40CrNiMoA steel and (b) Inconel 718 alloy.
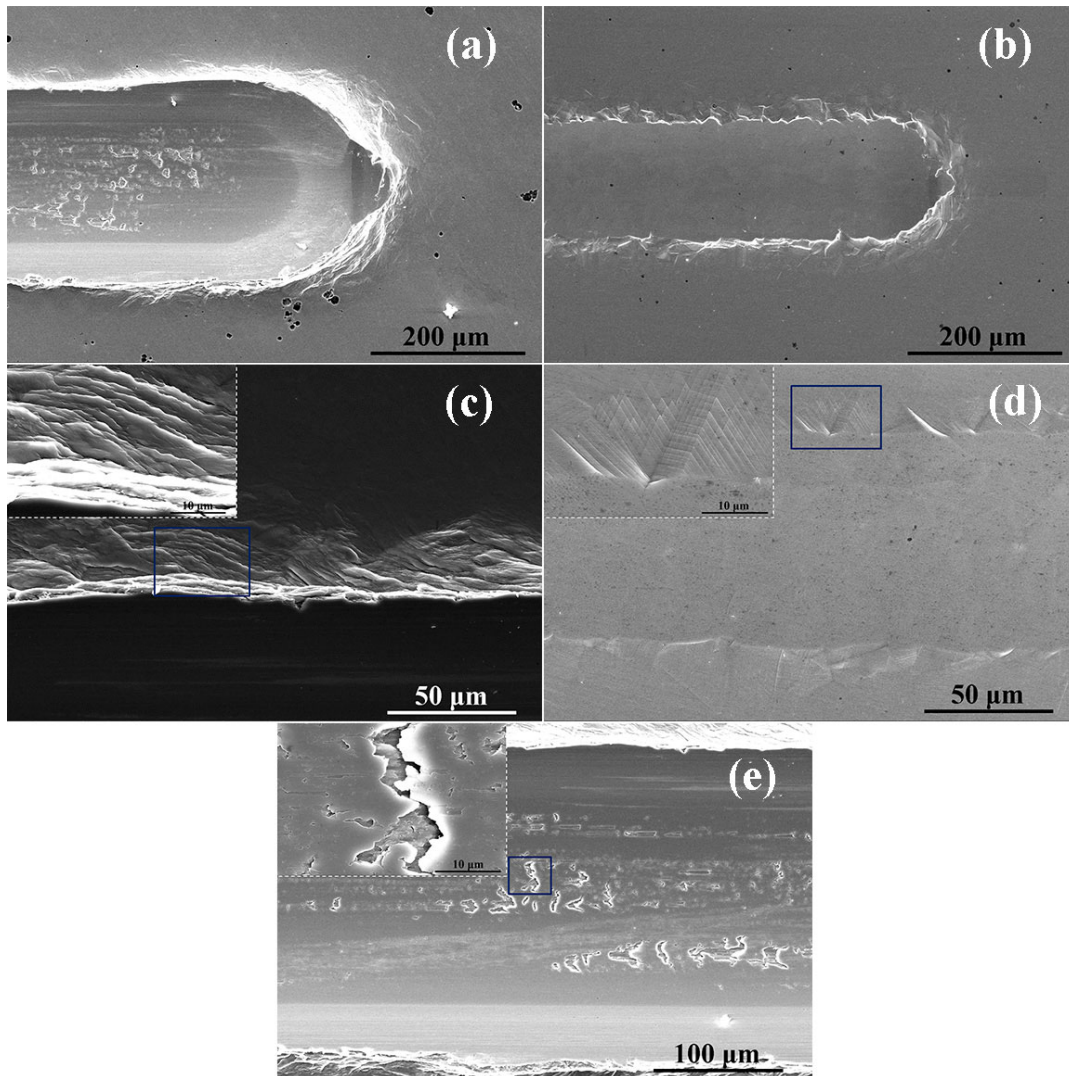
Fig. 4 SEM observation of the representative scratch tracks of (a, c, e) 40CrNiMoA steel and (b, d) Inconel 718 alloy.

seen that the testing temperature of 400 ℃ is a transition point during which the COFs for 40CrNiMoA steel and Inconel 718 alloy are close to each other. In the case of 40CrNiMoA steel, its COF drops drastically before 400 ℃ and the drop slows down at elevated temperatures. In contrast, the COF of Inconel 718 alloy decreases slowly before 400 ℃, and a quick decrease occurs after 400 ℃. These results imply temperature-mediated frictional features for two as-received alloyed materials, which are predominantly tailored by the developed tribolayer over the tribologically contacting surface [29].

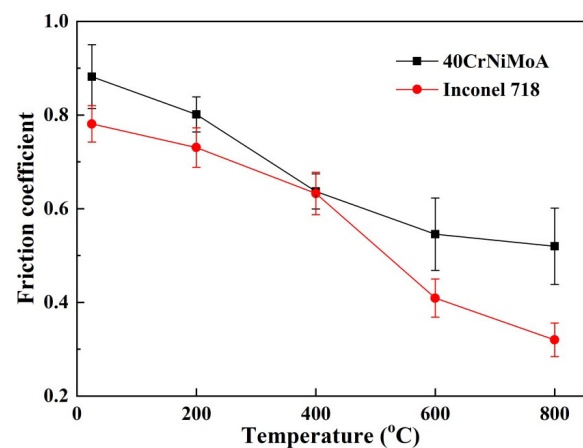During frictional tests at elevated temperatures, surface oxidation has a small influence on the

Fig. 5 Averaged coefficient of friction (COF) values of 40CrNiMoA steel and Inconel 718 alloy at different temperatures.

resulting friction and wear behavior. However, the quantification of oxidation by weighing the specimens after the test is inaccurate owing to its negligible change in mass [30, 31]. Thus, the specific wear rates of 40CrNiMoA steel and Inconel 718 alloy are measured using a surface profiler, as shown in Fig. 6(a). The wear behavior of the two alloys sliding against ceramic Si_3N_4 is temperature-dependent as well. The wear rate of 40CrNiMoA increases considerably with increasing temperature, which can likely be associated with the mechanical softening of 40CrNiMoA steel at elevated temperatures. The wear rate of Inconel 718 alloy displays a gradual decrease from RT to 600 ℃, although a further increase occurs at 800 ℃, which correlates with unexpected tribo-oxidation under the coupled temperature and stressed-shearing conditions. The specific wear rates of the Si_3N_4 counterpart of 40CrNiMoA steel and Inconel 718 alloy are plotted as a function of temperature in Fig. 6(b). All counterpart Si_3N_4 balls demonstrate similar wear behavior and reduction in wear when the temperature increases. In particular, minimum but equal wears appear for the Si_3N_4 counterparts at 800 ℃. This can be explained to be associated with the decreasing yield strengths, reduced hardness values, and increasing ductilities of the alloys themselves under the gradually increasing temperature. Thus, the wear damage is not dominant, whereas plastic deformation occurs at 800 ℃ [32]. However, the wear rate of the Si_3N_4

zcounterparts of the Inconel 718 alloy is less than that of 40CrNiMoA steel for a temperature range from RT to 600 ℃. As reported, the compacted oxidation layer often forms over silicon nitride during sliding, which is protective and able to resist wear [33]. It can be speculated that the tribolayer imparts a self-lubricating capability to silicon nitride. Further details are provided in the SEM/EDS analysis in Figs. 7 and 8 and Table 3.

3.3 Temperature-mediated wear transition

The microscopic characteristics of the worn surfaces of 40CrNiMoA steel and Inconel 718 alloy from 25 to 800 ℃ are shown in Fig. 7. The SEM micrographs show the removal of material fragments and some abrading action of oxidized wear debris by the evidence of some scoring marks and scattered debris on the 40CrNiMoA (Fig. 7(a)) and Inconel 718 alloy specimens (Fig. 7(f)), which yields higher friction between the rubbed contacts in Fig. 5. At 200 ℃, the predominant wear mechanism of 40CrNiMoA steel is abrasion, which is typical for a large quantity of wear debris and agglomeration of wear debris, as shown in Fig. 7(b); this is known as three-body abrasion. The Inconel 718 alloy demonstrates adhesion with distinguishable abrasion of oxidized wear debris and signs of debris compaction in Fig. 7(g).

The wear characteristics at 400 ℃ for the two as-received specimens significantly differ from those at RT and 200 ℃, as shown in Figs. 7(c) and 7(h). Oxide wear debris and high abrasive severity
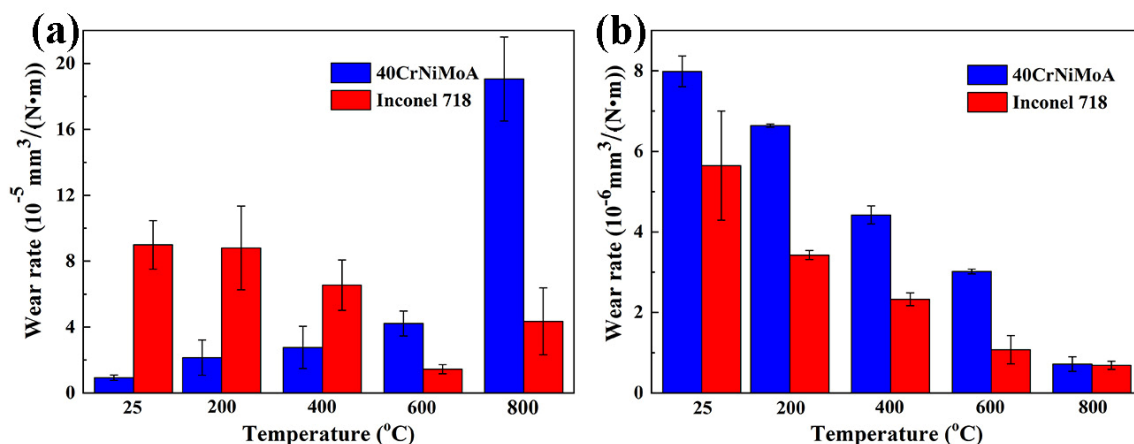

Fig. 6 Wear rate of (a) 40CrNiMoA steel and Inconel 718 alloy and (b) counterpart balls against the two materials at different temperatures.
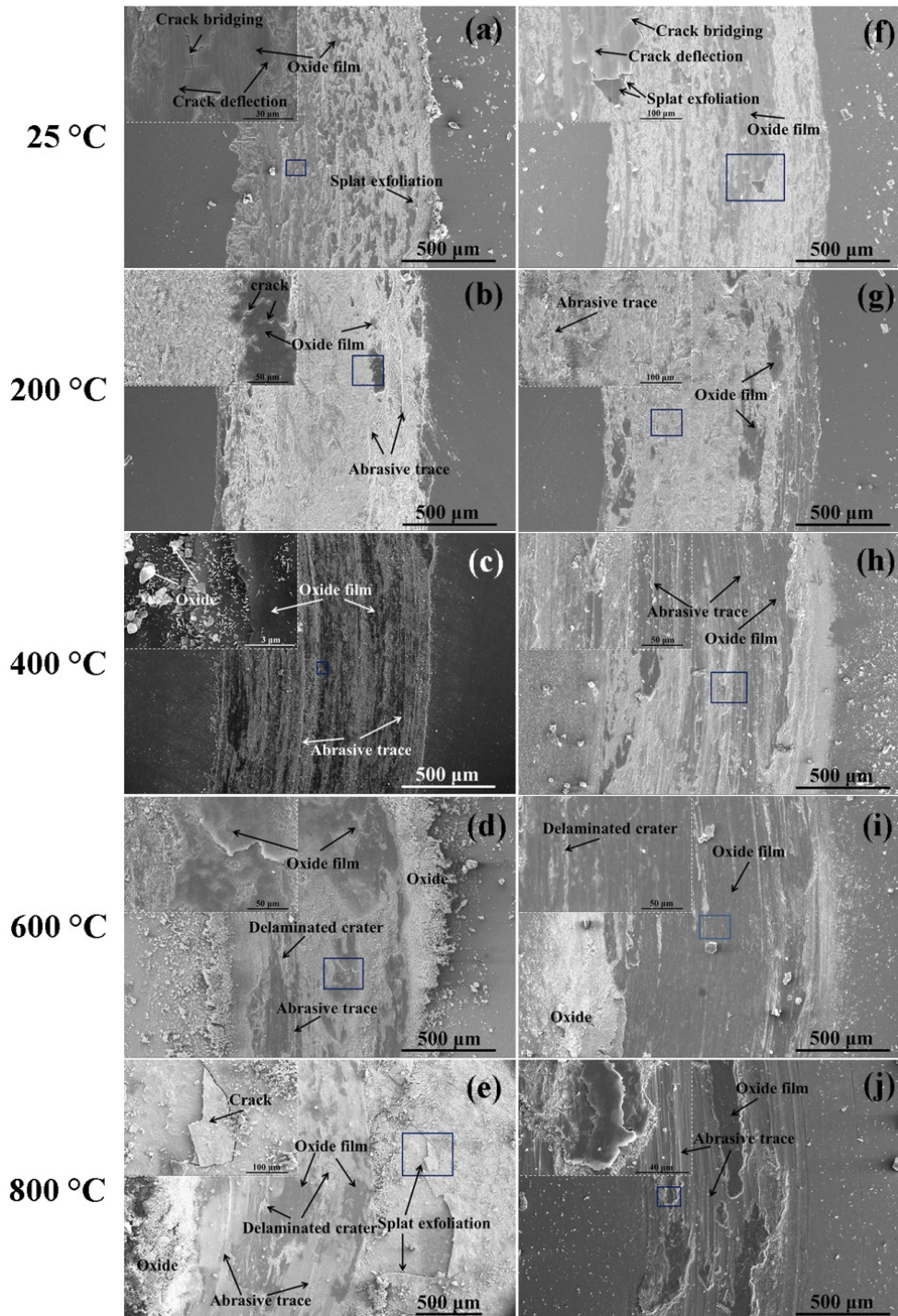
Fig. 7 SEM morphologies of worn scars and surfaces of (a–e) 40CrNiMoA steel, and (f–j) Inconel 718 alloy from RT–800 ℃.

can be found in the surrounding area of the wear track for 40CrNiMoA steel (Fig. 7(c)). A relatively smooth worn surface appears for the Inconel 718 alloy, where a compacted oxide film seemingly covers the surface (Fig. 7(h)). This can explain why

the Inconel 718 alloy demonstrates a significant reduction in friction [34]. In contrast, large amounts of oxide debris accumulated on both sides of the wear surfaces of the two materials at 600 ℃ (Figs. 7(d) and 7(i)), which is a typical

Table 3 Element contents (wt%) on the wear scar of Si_3N_4 counterparts against 40CrNiMoA steel and Inconel 718 alloy.

	40CrNiMoA steel (℃)					Inconel 718 alloy (℃)				
	25	200	400	600	800	25	200	400	600	800
N	—	—	—	—	—	—	—	—	—	—
O	—	—	—	—	—	—	—	—	—	—
Al	2.31	2.26	2.27	0.08	1.89	2.45	2.20	1.27	1.73	1.15
Si	71.78	69.55	64.79	53.73	69.65	70.72	70.72	81.25	63.38	75.55
Nb	24.13	26.30	30.02	35.28	26.17	23.86	24.39	15.42	24.78	14.36
Mo	0.10	0.21	0.83	8.85	0.09	0.26	0.28	0.42	0.45	0.30
Ti	1.61	1.47	1.08	1.16	1.39	1.65	1.31	0.81	1.42	0.62
Cr	0.01	0.02	0.11	0.14	0.03	0.13	0.13	0.11	1.80	0.93
Fe	0.03	0.14	0.63	0.56	0.74	0.18	0.20	0.13	1.99	1.88
Ni	0.03	0.07	0.27	0.20	0.03	0.74	0.77	0.57	4.33	5.20

Note: – indicates that it is not detected.

feature of serious abrasion. Such delaminated craters can be found within the wear scars. The microscopic view further shows the different morphologies of the compacted oxide film on the wear surfaces of 40CrNiMoA steel and Inconel 718 alloy, where the oxide film is relatively loose and has poor adherence to 40CrNiMoA steel in Fig. 7(d) and is highly compacted for the Inconel 718 alloy in Fig. 7(i). The governing mechanisms at 800 ℃ for 40CrNiMoA steel are agglomeration of oxides and delaminated craters as well as serious exfoliation of the oxide layer in Fig. 7(e), which indicates that oxide is transferred to the opposite side [1]. The wear mechanism of the Inconel 718 alloy is mainly adhesive with severe scoring marks, as shown in Fig. 7(j). However, this oxide layer renders superior lubrication at elevated temperatures, thereby significantly reducing friction, as shown in Fig. 5. The transition in wear mechanism from 25 to 800 ℃ for 40CrNiMoA steel and Inconel 718 alloy is summarized in Table 4. As observed, a loose, compact layer is formed at 600 ℃ for 40CrNiMoA steel (Fig. 7(d)), whereas a dense oxide layer is formed at 200℃ for the Inconel 718 alloy (Fig. 7(g)), which is consistent with the COFs of the two materials in Fig. 5.

Microscopic observation of the worn surfaces of Si_3N_4 was also carried out using SEM, as shown in Fig. 8. As the temperature increases, the diameters of the wear scars on the paired Si_3N_4 surface against 40CrNiMoA steel and Inconel 718 alloy become smaller, which is associated with the

self-lubricating nature and thus the wear resistance of the progressively grown tribolayer on the paired Si_3N_4 surface. At room and ambient temperatures, the worn surfaces are smooth, and abrasive grooves are visible, with the scattering of fine debris over silicon nitride against 40CrNiMoA steel shown in Figs. 8(a) and 8(b). When sliding against Inconel 718 alloy, debris and grooves occur along the sliding direction, which is clear evidence of abrasive wear. The worn surfaces are also relatively rough (Figs. 8(f) and 8(g)). Although this debris sometimes clumps together, there are many single particles scattered over the worn surface. At 400 ℃, many more particulate materials can be found at the trailing edge of the worn Si_3N_4 surface against 40CrNiMoA steel (Fig. 8(c)) and against

Table 4 Wear mechanisms of 40CrNiMoA steel and Inconel 718 alloy at different temperatures.

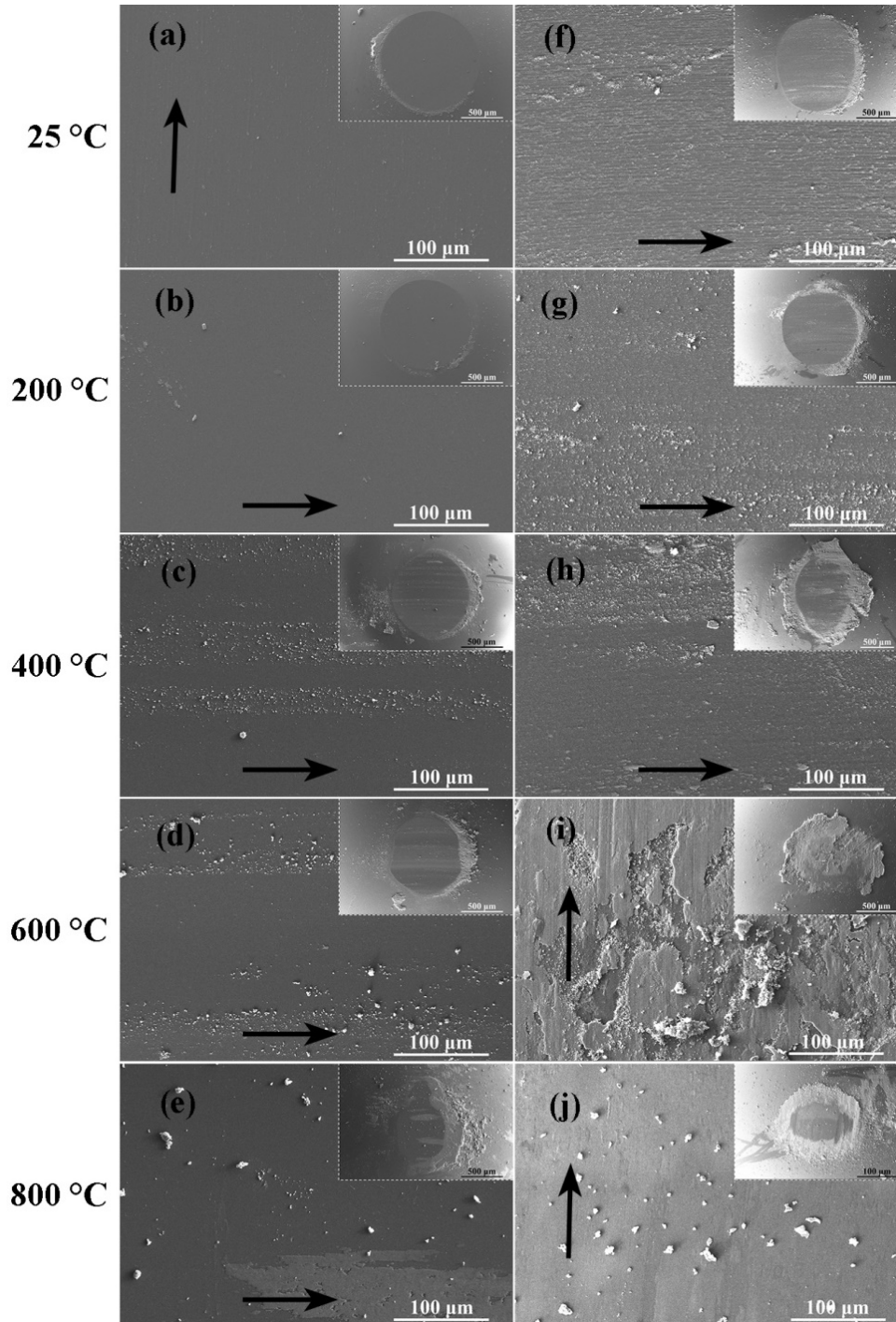|	40CrNiMoA steel	Inconel 718 alloy
25 ℃	Oxidation and abrasion	Oxidation and abrasion
200 ℃	Oxidation and abrasion	Abrasion and debris compaction
400 ℃	Oxidation and serious abrasion	Compacted oxide film
600 ℃	Serious Abrasion and Foose compacted oxide film	Compacted oxide film
800 ℃	Agglomerated oxides and compacted oxide film	Adhesive and compacted oxide film

Fig. 8 SEM morphologies of worn scars over Si_3N_4 counterparts: (a–e) 40CrNiMoA steel, and (f–j) Inconel 718 alloy from RT–800 ℃; arrows indicate sliding directions.

Inconel 718 alloy (Fig. 8(h)).

Nevertheless, the worn topographies at 600 ℃ are significantly different from those at relatively lower temperatures (Figs. 8(d) and 8(i)). There are accumulations of fine debris particles, some

relatively adherent on the Si_3N_4 sliding surface against 40CrNiMoA steel, as shown in Fig. 8(d); instead, severe adhesion and abrasive grooves are present under the Inconel 718 alloy-mated conditions shown in Fig. 8(i), where the structure

undergoes a process of severe plastic deformation. At 800 ℃, when wear is relatively low, smooth tribolayers are constructed over the worn silicon nitride against 40CrNiMoA steel (Fig. 8(e)) and Inconel 718 alloy (Fig. 8(j)). This thin layer separates the rubbing surfaces and reduces friction.

3.4 SEM/EDS identification of worn surfaces

EDS line analyses across the worn surfaces of 40CrNiMoA steel in Figs. 9(a)–9(e) show the visible silicon within the worn surface at room/ ambient temperatures, due to material transfer. EDS line analyses across the worn surfaces of Inconel 718 alloy (Figs. 9(f)–9(j)) demonstrates similar characteristics; all worn surfaces include a significant amount of oxygen, which definitely affirms intensive oxidation during sliding. A careful comparison of the oxygen intensity, as shown in Fig. 9, shows that the oxygen concentration within the central contacting area is much higher than those at both edges of the wear track with the exception of Figs. 9(d), 9(e), and 9(j), which arises from the accumulation of abrasive debris during the thermomechanical process. Note that 40CrNiMoA steel is more severely oxidized than the Inconel 718 alloy. Although it is relatively difficult to determine the accurate extent of oxidation, oxidation intensifies with temperature within and outside the worn surface [35], and 40CrNiMoA steel is more severely oxidized than the Inconel 718 alloy because of the lack of Cr in the former [36].

The elemental distributions inside and outside the wear tracks of 40CrNiMoA steel and Inconel 718 alloy are shown in Figs. 10 and 11, respectively. In comparison, the abrasion of Fe_2O_3 decreases as temperature increases from RT to 800 ℃, whereas it behaves as a lubricant at elevated temperatures. Another noticeable feature is increasing molybdenum concentration within the worn area in response to increasing temperature, which indicates that molybdenum oxide significantly contributes to the frictional decrement at elevated
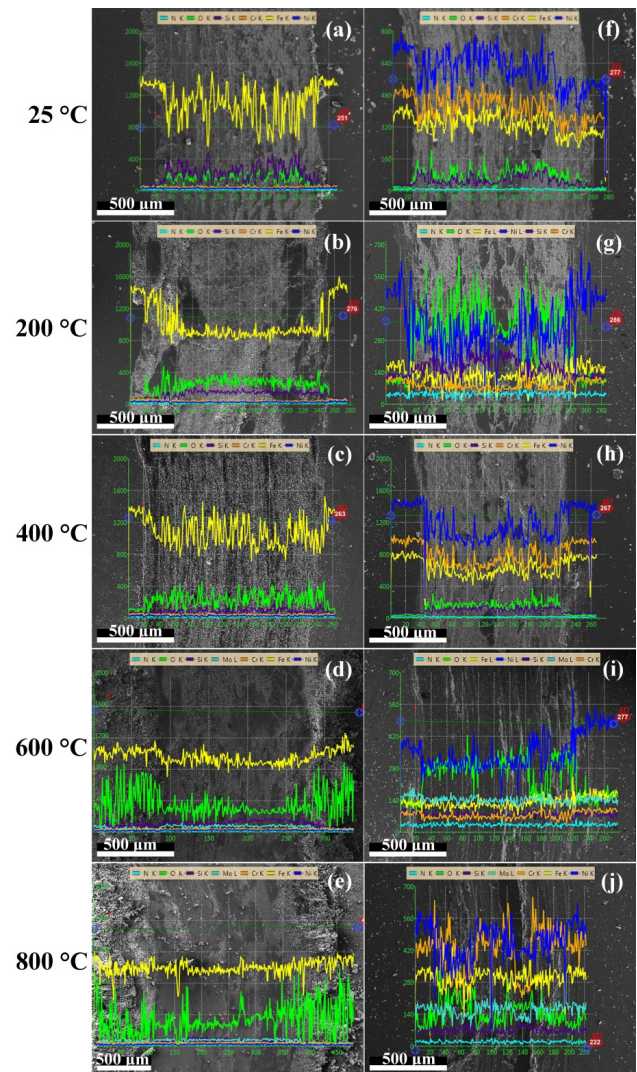

Fig. 9 EDS line analyses of element content on the wear surface of (a–e) 40CrNiMoA steel and (f–j) Inconel 718 alloy from RT–800 ℃.

temperatures.

A similar distributional characteristic of Fe can be observed inside and outside the wear tracks of Inconel 718 alloy (Fig. 11) compared to that of 40CrNiMoA steel. In particular, the increasing accumulation of Mn, N, and Nb within the wearing region is seemingly homogeneous, especially at 800 ℃. In contrast, the distributions of Cr and Ni are more dominant in the central wearing area, which imply that the temperature-dependent tribological behavior of the Inconel 718 alloy is associated with the formation of a lubricating surface primarily
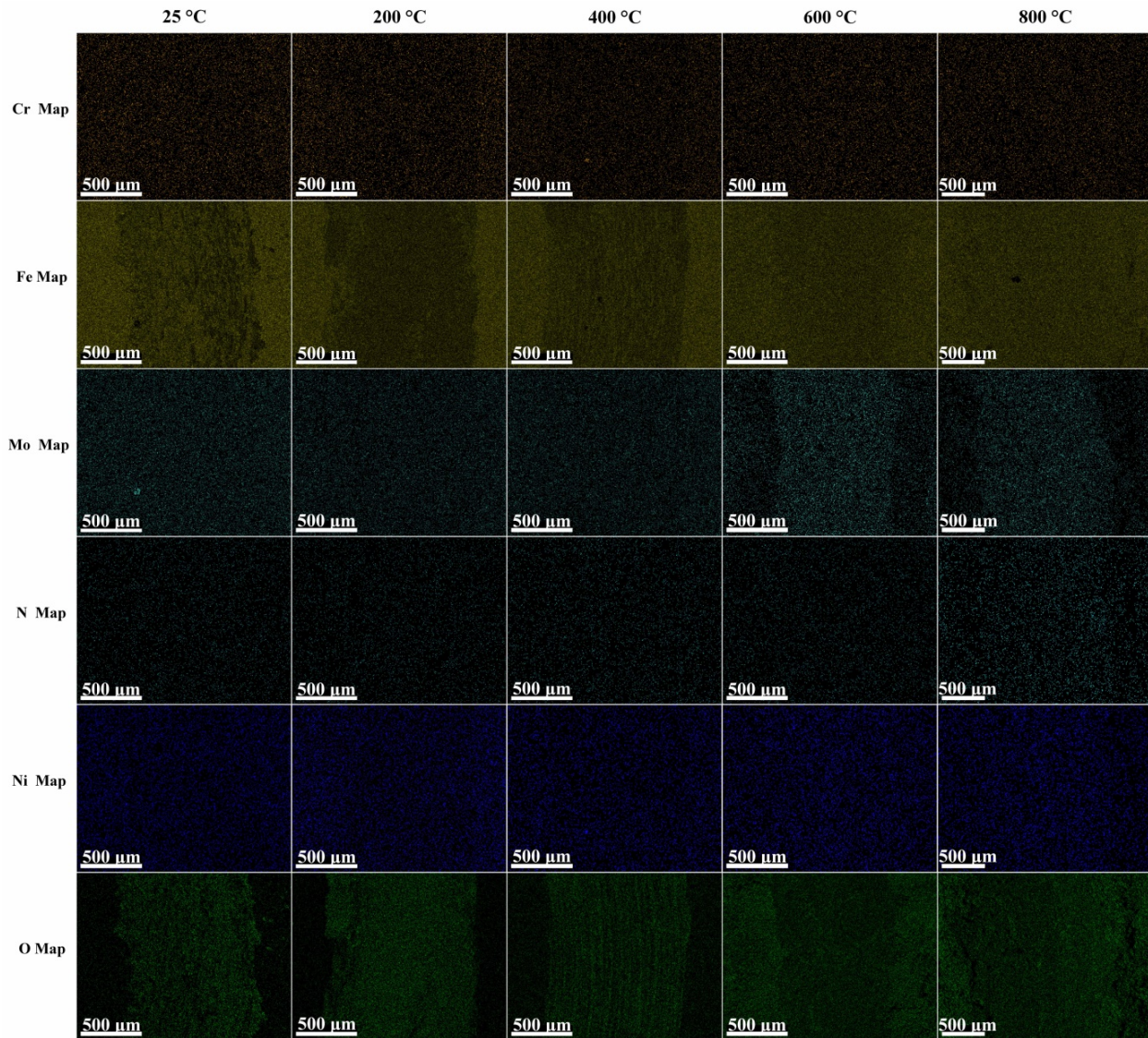
Fig. 10 Elemental distribution maps of 40CrNiMoA steel from RT–800 ℃.

composed of Fe, Cr, and Ni.

An EDS mapping analyses are conducted on the counterparts sliding against 40CrNiMoA steel and Inconel 718 alloy (Fig. 12). For Si$_3$N$_4$ paired with 40CrNiMoA steel, EDS mapping proves that a large amount of Fe is transferred onto the worn Si$_3$N$_4$ surface with intensive oxidation (Fig. 12(b)). When sliding against Inconel 718 alloy, the Fe, Cr, Ni, Mo, and O are distinguishable on the worn Si$_3$N$_4$ surface, as shown in Figs. 12(f)–12(o). EDS analysis reveals a fraction of material transfer and thereby a tribochemical layer with lubricating ability on the Si$_3$N$_4$ surface.

It is clear that material transfer occurs, and a compact oxide layer covers the worn Si$_3$N$_4$ surface when it matches the Inconel 718 alloy at 800 ℃. This layer is made up of Fe, Cr, Ni, Mo, and O. However, once the tribo-oxide layer is too thick, it separates easily and wears away [37], causing a sudden increase in wear loss at 800 ℃, as shown in Fig. 6(a).

It has been acknowledged that material transfer facilitates the restoration of the contacting surface by constructing a lubricant layer primarily consisting multiple oxides, thus reducing friction and improving the wear resistance. As shown in Table 3, when sliding against Inconel 718 alloy, the dominant elements on the wear scar of Si$_3$N$_4$ are
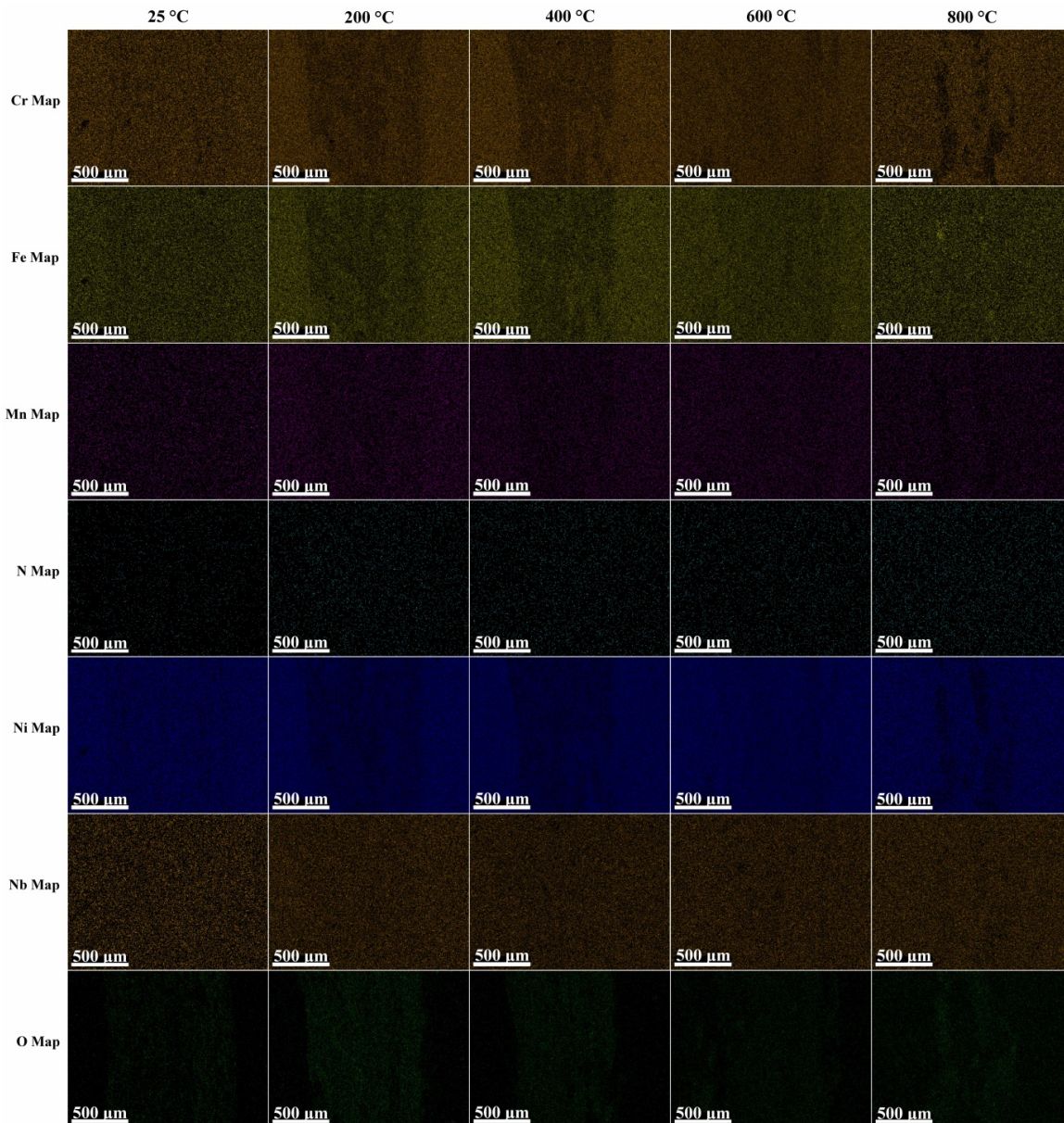
Fig. 11 Elemental distribution maps of Inconel 718 alloy from RT–800 ℃.

Mo, Ni, Cr, and Fe, while the Si₃N₄ counterparts sliding against 40CrNiMoA steel show the transfer of Mo, Ni, and Fe. The different wear rates of Si₃N₄ are intrinsically associated with the composition of the tribolayer due to material transfer. Thus, the difference in the constituents of the tribolayer leads to the resulting wear variety of Si₃N₄ counterparts against Inconel 718 alloy and 40CrNiMoA steel, as shown in Fig. 6(b). However, it was barely detectable for N and O elements on the wear scars of S₃N₄ counterparts against

40CrNiMoA steel and Inconel 718 alloy, respectively. It is true that the analysis of the N by EDS is generally regarded as qualitative and for informative purposes only because of its low fluorescence yield, absorption, and peak overlaps with higher elements in the L, M, and N lines [38]. In the case of O, the amount of O is definitely present within the transfer layer, but it is much lower than the resolution (0.1%) of the EDS equipment used in this study [39]. Thus, the contents of N and O are not provided in Table 3.
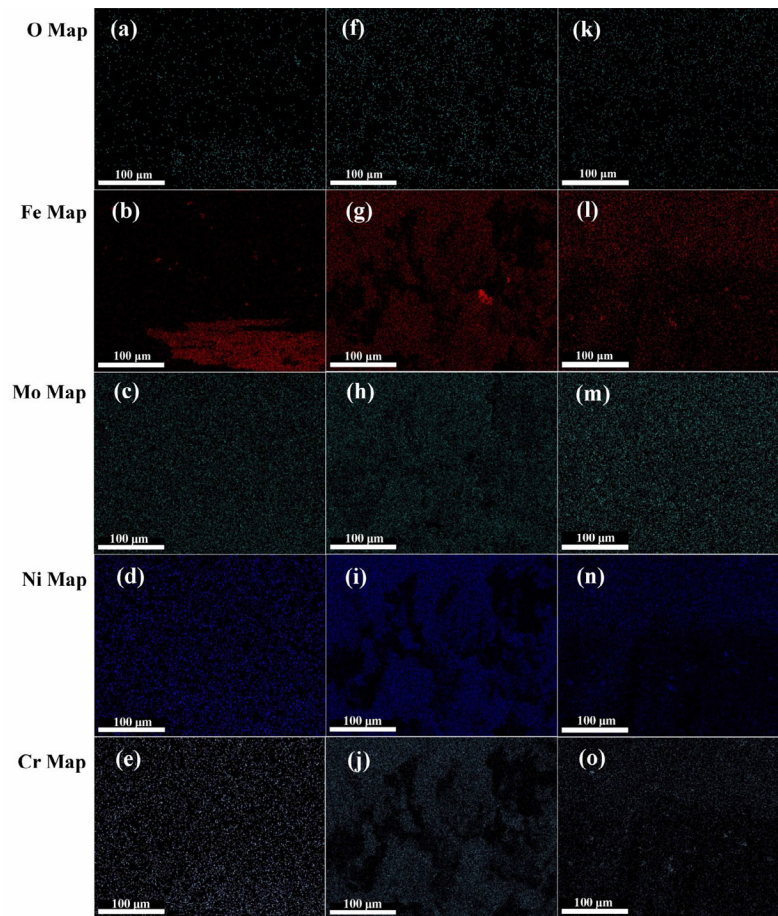
Fig. 12 Elemental distribution maps on the worn Si_3N_4 surface against (a–e) 40CrNiMoA steel at 800 ℃, (f–j) Inconel 718 alloy at 600 ℃, and (k–o) Inconel 718 alloy at 800 ℃.

3.5 Raman analysis of the inside and outside the wear track

The phase composition inside and outside the worn surface of 40CrNiMoA steel and Inconel 718 alloy are analyzed by micro-Raman spectroscopy (Fig. 13). The observations confirm that the oxide phase occurs within the worn surface and is corroborated by comparison with the oxides on the outer worn surface, which stem from static oxidation. For the 40CrNiMoA steel, MoO_3, Fe_2O_3, and MnO_2 are present outside the worn region in Fig. 13(a), which can be identified by the representative peaks at 290, 411, and 1,319 cm⁻¹, respectively [40–42]. This is associated with the oxidation kinetics of individual elements within 40CrNiMoA steel [43]. However, these peaks are still observable for the inner worn area (Fig. 13(b)) and are more intense and narrower with

increasing temperature, which is due to the increasing crystallinity and grain coarsening of the oxide formed in the wear track [44]. Thus, friction-induced changes in the composition of a surface layer occur. At relatively low temperatures, hard Fe_2O_3 debris and the oxygen-absorber Mn readily create a preventive layer on the sliding surface, a typical mechanism of oxidative wear accompanied with medium abrasion (Figs. 7(a, b) and 8(a, b)), which reduces wear, as demonstrated in Fig. 6(a). When the sliding test exceeds 400 ℃, significantly more MoO_3 gradually appears on the worn surface and restores the amount of contact between the rubbed pairs, thereby lowering friction and inhibiting wear. As reported, MoO_3 is a volatile compound that is constantly ground into the worn surface [45, 46]. It prefers to interact with surrounding media and forms molybdate; nevertheless, this compound is scarcely detected
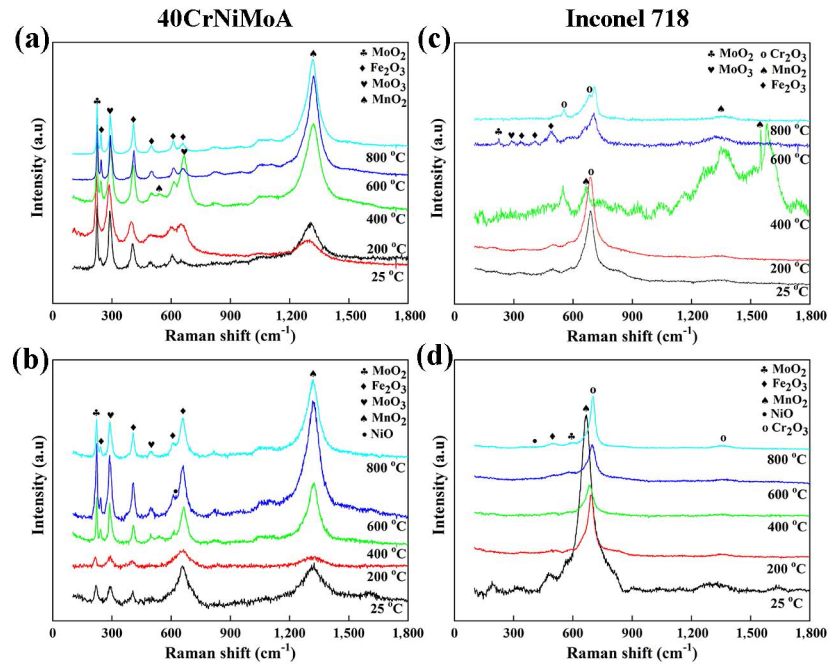
Fig. 13 Raman spectra of (a, c) unworn surface and (b, d) worn area of the two materials from RT–800 ℃.

in this study.

Inconel 718 alloy includes various alloying constituents that influence oxidation during the static heat treatment and sliding. As shown in Fig. 13(c), at room/ambient temperatures, a layer mainly comprising Cr_2O_3 is formed on the Inconel 718 alloy. Some duplex oxides such as spinel $NiFe_2O_4$ simultaneously exist near the surface [47, 48]. As the temperature is above 400 ℃, in addition to Cr_2O_3, significantly more MnO_2 emerges, where the Raman peaks at 685 and 663 cm^{-1} are assigned to Cr_2O_3 and MnO_2, respectively [49, 50]. However, if the temperature is increased to 800 ℃, the surface will not only contain a significant amount of Cr_2O_3, but it will also contain a minimal amount of oxides of other alloying constituents, which is attributed to the superior protection of the Cr_2O_3 layer on Inconel 718 alloy, which effectively limits the inward attack of oxygen and is simultaneously supported by the lower outward diffusion rate of Cr ions [51–53].

Nevertheless, there is a significant variation in the composition of the worn surface shown in Fig. 13(d). At RT, ferric oxide located at 498 cm^{-1} [54] and manganese oxide phase are mainly

responsible for the low friction, where the MnO_2 emerging facilitates surface smoothening [55]. As a comparison, completely different oxides within the worn surface are formed at elevated temperatures. For example, at 800 ℃ the dominant formation of the Cr_2O_3 layer is the main reason for the lower friction and wear observed in Figs. 5 and 6(a). The varying degree of oxidation of Inconel 718 alloy, along with the forms of the resulting oxides on the solid surface, are strongly influenced by temperature as well as the surface chemistry during friction, resulting in a significant change in friction and wear.

3.6 Justification of tribo-oxidation and static oxidation

The oxide films inside and outside the worn surface of the two as-received materials are depicted as observed from the cross-section view in Fig. 14. The common feature of increasing thickness with temperature elevation is clearly distinguishable: at room/ambient temperatures, abrasive oxide grains are ground onto the worn area, while static oxidation is barely identifiable for the two as-received materials because the
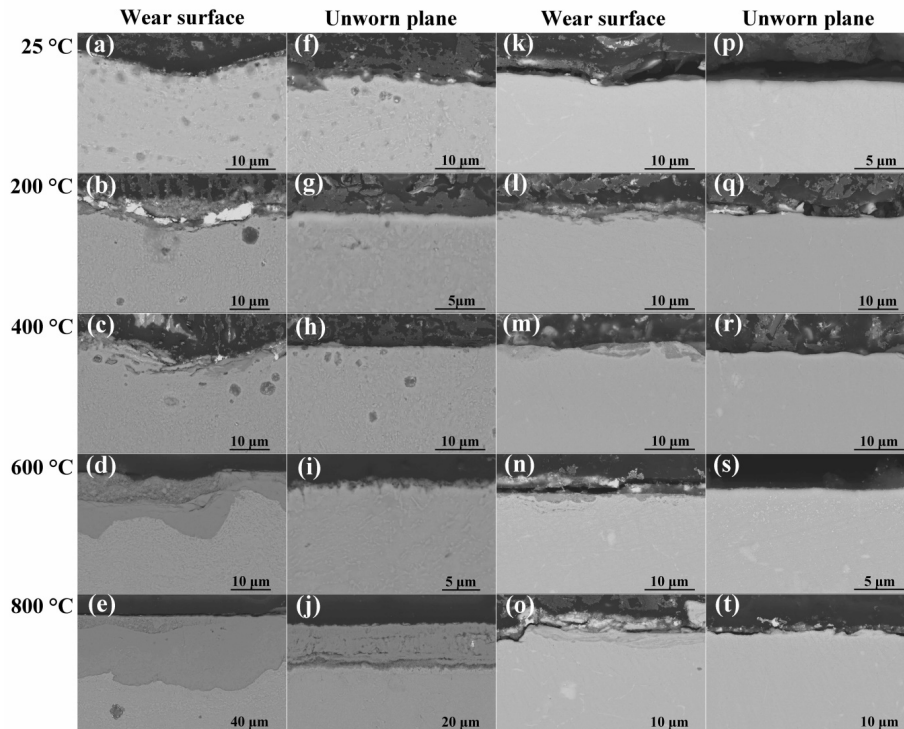
Fig. 14 SEM cross-section micrographs of oxide layers of (a–j) 40CrNiMoA steel and (k–t) Inconel 718 alloy at different temperatures.

temperature does not exceed 400 ℃. Generally, approximately 500-nm-thick-fine oxide film deposits on the rubbed metallic surface at lower temperatures [56] and behaves as either positive abrasion or undesired three-body action [57]. It can be concluded that the stressed-shearing action during friction augments the growing oxides within the worn area [58]. In particular, as the temperature reaches 600 ℃, a static oxide layer on 40CrNiMoA steel is observable, approximately 1.3 μm thick in Fig. 14(i), and the average thickness of the oxide layer up to 12.1 μm can be found within the wear track in Fig. 14(d). At 800 ℃ the oxide layer within the worn surface of 40CrNiMoA steel is very thick, approximately 41.3 μm in Fig. 14(e), while the static oxidative products have a thickness of approximately 18.4 μm in Fig. 14(j).

The Inconel 718 alloy demonstrates a discontinuous oxide film with a maximum average thickness of 1 μm within the wear track, which further reflects dominant abrasive grooves present at room/ambient temperatures. As the temperature increases to 800 ℃, an oxide layer about 2.3 μm thick can be clearly observed within the worn area in Fig. 14(o).

Compared with the static oxidation of 40CrNiMoA steel, only mild oxidation occurs inside and outside the worn surface, which is reported to be related to the presence of dense Cr_2O_3 [59], which prevents Inconel 718 alloy from wear and oxidative corrosion. This can be further evidenced by the absence of the oxide film at RT in Fig. 14(p), and the presence of a thin oxide film less than 1 μm during static oxidation at 800 ℃ as shown in Fig. 14(t). The images reveal that the frictional process accelerates the growth of the oxide film as compared to static oxidation.

Raman spectra collected from inside and outside the worn surface illustrate the variation in the chemical composition of the developing oxide surface in response to temperature. The difference in the oxide layer inside and outside the wear track is further clarified in Fig. 13. As reported by Wahl et al. [60], metal oxides become soft when the temperature falls within 0.4–0.7 of the absolute melting temperature. It is noted that softened MnO_2 preferentially adheres to the wear track at higher contact temperatures, where Mn has much higher mobility and needs more oxygen for

stabilization than those of other alloying elements such as Fe [61]. Thus, we observed intense peaks corresponding to MnO_2 on the worn surface for the two alloyed materials.

3.7 Discussion

According to the theories of oxidational wear [62, 63], the tribological characteristics depend on the chemical and mechanical properties of the resulting oxides, their thicknesses and adherences over the sliding surface, wearing variations, and surface roughness values of the contacting surfaces. In general, the friction-induced rise in temperature accelerates the oxidation of the sliding surface. If the oxide film has low shearing strength, it enables effective lubrication between the rubbing surfaces, thereby reducing friction and wear. Normally, a film with sufficient thickness and good adherence can separate the solid surfaces from contact and thus inhibit wear [64]. Instead, the comparatively harder oxide particles behave as an abrasive medium that causes an unwanted wear increase. Coupled stressed-shearing and temperature during friction critically affect the heat generation/dissipation, interfacial temperature, and kinetics of oxide film formation and its composition [65]. The exact nature of the variation in wear rate and COF with temperature is largely dependent upon the underlying wear mechanisms, during which the restoration of oxide debris over the sliding surface is critical. The morphological identification in Section 3.3 indicates the formation of a tribo-oxide surface with multiple steps, for example, the fragmentation of wear debris and its subsequent oxidation, followed by agglomeration and compaction. If the temperature is sufficiently high, the tribo-oxide debris can be sintered, forming a shiny glaze layer. This glaze layer has been reported to be effective to reduce friction and prevent wear, particularly in nickel-based alloy systems [66–68]. In this study, similar characteristics were also found. A plot of temperature, COF, and wear rate is shown in Fig. 15.

The COF decreases with the increase in operational temperature, as shown in Fig. 15. A similar tendency in the wear rate and friction can be observed due to the temperature, which is
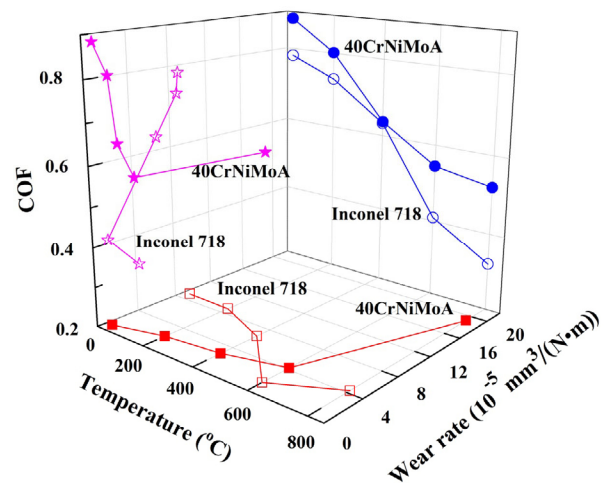

Fig. 15 Changes in temperature, wear rate, and COF.

largely dependent on the formation of the tribo-oxide film, as discussed in Section 3.3. SEM/EDS analysis of worn surfaces further supported these observations. With increasing temperatures, the interaction of the resulting oxides and the softening process of the materials themselves substantially determines the tribological performance; thus, the material demonstrates different tribological responses in Figs. 5 and 6. The tribo-induced oxide layer is mostly reported to deliver lubrication and contributes to a lower COF and wear rate [33]. However, although COF decreases, the metallic matrix inherently softens at elevated temperatures, resulting in an increase in wear. In this study, no mechanical value at elevated temperature is present, but it is true that the sliding surface softens due to temperature, which alters the adhesion between the tribo-oxide film and the substrate. This increases the fracturing possibility of the tribo-oxide film. As shown in Figs. 7(e) and 7(f), delamination cracking is closely associated with thermal shock stresses induced by the mismatch in the thermal expansion of carbides and oxides [69]. Normally, the friction between two unlubricated surfaces arises owing to adhesion and plowing, where the plowing component plays a critical role in abrasive wear. If fine abrasive particles are present, the adhesion component can play an important role in influencing COF [70, 71]. At lower temperatures, the abrasive wear mechanisms are dominated by the plowing processes. At higher

temperatures, the wear process is dominated by the oxidative wear, during which a relatively thick oxide film reduces the true area of contact. The corresponding decrease in COF at elevated temperatures is shown in Fig. 5.

Under the surrounding conditions, a very thin oxide layer is often present on metallic surfaces. For instance, even after polishing, specimens often have an oxide thickness of several nanometers. However, a thick oxide layer grows up to several microns during friction, as shown in Fig. 14, compared with static oxidation. This demonstrates the significance of the stressed-shearing action, which accelerates the oxidation during friction. In particular, a higher contact temperature promotes oxidative kinetics during sliding. However, if the oxide layer is too thick, it will break up and form particles [37]. Consequently, the wear rate depends significantly on the oxidation. The inconsistency in the correlation between the friction and wear of the two alloyed materials can be attributed to the change in the contribution of surface chemistry and mechanical properties with varying temperature [69, 70]. The results of the present work are fairly consistent with earlier observations on coated and uncoated specimens [72, 73].

4　Conclusions

This study focused on the effect of temperature on the friction and wear characteristics of 40CrNiMoA steel and Inconel 718 alloy when sliding against a ceramic Si_3N_4 counterpart in order to clarify the role of tribo-oxidation and thermal-induced oxidation in tribological capabilities. The COF and abrasive wear rates of the two as-received materials decrease with increasing temperature. When paired with ceramic silicon nitride, the superior mechanical strength of Inconel 718 alloy to that of 40CrNiMoA steel is considered to be mainly responsible for the lower wear rate of the Inconel 718 alloy/Si_3N_4 pair at lower temperatures. At elevated temperatures, reduced wear and COF for the Inconel 718 alloy/Si_3N_4 pair results from the formation of a lubricating oxide film consisting of Cr_2O_3, whereas

the tribochemical layer with a simultaneous softening feature of the material base leads to lower friction but higher wear. Stressed-shearing action during friction accelerates oxide growth within the worn area. Thus, the tribo-induced oxidation plays a dominant role in the tribological performance across a wide range of temperatures. However, thermally induced oxidation and softening of the materials themselves become important with increasing temperature, and thereby contribute to the transition in tribology. The variations in wear and COF are intrinsically associated with varying composition on the solid surface, which can be attributed to the competition between tribo-chemical oxidation, thermally induced oxidation, and softening.

Author contributions

S Wan conceived, designed the study, reviewed the edited manuscript. L Bai performed the experiments and drafted the manuscript. G Yi and Y Shan provided the raw materials and technical support, S T Pham and A K Tieu reviewed and edited the manuscript, Y Li and R D Wang provided two alloys in this study. All authors read and approved the manuscript.

Acknowledgements

References

[1] Barrau O, Boher C, Vergne C, Rezai-Aria F, Gras R. Investigations of friction and wear mechanisms of hot forging tool steels. In *6th International Tooling Conference*, Karlstad, Sweden, 2002: 81–94.

[2] So H, Chen C T, Chen Y A. Wear behaviours of laser-clad stellite alloy 6. *Wear* **192**(1–2): 78–84 (1996)

[3] Wang X J, Yao X M, Zhang H, Liu X J, Huang Z R. Microstructure and tribological performance of mesocarbon microbead–silicon carbide composites. *Materials* **12**(19): 3127 (2019)

[4] Torgerson T B, Mantri S A, Banerjee R, Scharf T W. Room and elevated temperature sliding wear behavior and mechanisms of additively manufactured novel precipitation strengthened metallic composites. *Wear* **426–427**: 942–951 (2019)

[5] Du L M, Lan L W, Zhu S, Yang H J, Shi X H, Liaw P K, Qiao J W. Effects of temperature on the tribological behavior of $Al_{0.25}$CoCrFeNi high-entropy alloy. *J Mater Sci Technol* **35**(5): 917–925 (2019)

[6] Wan S H, Tieu A K, Xia Y N, Zhu H T, Tran B H, Cui S G. An overview of inorganic polymer as potential lubricant additive for high temperature tribology. *Tribol Int* **102**: 620–635 (2016)

[7] Dhanasekaran S, Gnanamoorthy R. Abrasive wear behavior of sintered steels prepared with MoS_2 addition. *Wear* **262**(5–6): 617–623 (2007)

[8] Hernandez S, Hardell J, Winkelmann H, Ripoll M R, Prakash B. Influence of temperature on abrasive wear of boron steel and hot forming tool steels. *Wear* **338-339**: 27–35 (2015)

[9] Pearson S R, Shipway P H, Abere J O, Hewitt R A A. The effect of temperature on wear and friction of a high strength steel in fretting. *Wear* **303**(1–2): 622–631 (2013)

[10] Österle W, Urban I. Friction layers and friction films on PMC brake pads. *Wear* **257**(1–2): 215–226 (2004)

[11] Reddy K M, Mukhopadhyay A, Basu B. Microstructure-mechanical-tribological property correlation of multistage spark plasma sintered tetragonal ZrO_2. *J Eur Ceram Soc* **30**(16): 3363–3375 (2010)

[12] Thirugnanasambantham K G, Raju R, Sankaramoorthy T, Velmurugan P, Kannagi A, Reddy M C K, Chary V S K, Mustafa M A, Chandra V R. Degradation mechanism for high-temperature sliding wear in surface-modified In718 superalloy. *Cogent Eng* **5**(1): 1501864 (2018)

[13] He Q, Li A L, Qu W H, Zhang Y, Wang T, Kong L H. Investigation on friction and wear properties of high-temperature bearing steel 9Cr18Mo. *Mater Res* **21**(3): e20170715 (2018)

[14] Jing X T, Lou B Z, Shen F S. Fatigue crack growth and crack closure behavior of the CrNiMo steels at negative stress ratio. In *Proceedings of the 7th International Conference On Fracture (ICF7)*. Salama K, Ravi-chandar K, Taplin D M R, Rao P R, Eds. Amsterdam: Elsevier, 1989: 1187–1194.

[15] Grzesik W, Niesłony P, Habrat W, Sieniawski J, Laskowski P. Investigation of tool wear in the turning of Inconel 718 superalloy in terms of process performance and productivity enhancement. *Tribol Int* **118**: 337–346 (2018)

[16] Liu W C, Yao M, Chen Z L, Wang S G. Niobium segregation in inconel 718. *J Mater Sci* **34**(11): 2583–2586 (1999)

[17] Azadian S, Wei L Y, Warren R. Delta phase precipitation in Inconel 718. *Mater Character* **53**(1): 7–16 (2004)

[18] Liang H Q, Zeng Y P, Zuo K H, Xia Y F, Yao D X, Yin J W. Mechanical properties and thermal conductivity of Si_3N_4 ceramics with YF_3 and MgO as sintering additives. *Ceram Int* **42**(14): 15679–15686 (2016)

[19] Whitenton E P, Blau P J. A comparison of methods for determining wear volumes and surface parameters of spherically tipped sliders. *Wear* **124**(3): 291–309 (1988)

[20] Varga M, Rojacz H, Winkelmann H, Mayer H, Badisch E. Wear reducing effects and temperature dependence of tribolayer formation in harsh environment. *Tribol Int* **65**: 190–199 (2013)

[21] Sangwal K, Surowska B, Błaziak P. Analysis of the indentation size effect in the microhardness measurement of some cobalt-based alloys. *Mater Chem Phys* **77**(2): 511–520 (2003)

[22] Petrík J, Palfy P. The influence of the load on the hardness. *Metrol Meas Syst* **18**(2): 223–234 (2011)

[23] Guo E Y, Singh S S, Kaira C S, Meng X Y, Xu Y J, Luo L

S, Wang M Y, Chawla N. Mechanical properties of microconstituents in Nb-Si-Ti alloy by micropillar compression and nanoindentation. *Mater Sci Eng A* **687**: 99–106 (2017)

[24] Kalkhoran S M, Choi W B, Gouldstone A. Estimation of plastic anisotropy in Ni-5% Al coatings via spherical indentation. *Acta Mater* **60**: 803–810 (2012)

[25] Wang M Z, Wu J J, Wu H F, Zhang Z K, Fan H. A novel approach to estimate the plastic anisotropy of metallic materials using cross-sectional indentation applied to extruded magnesium alloy AZ31B. *Materials* **10**(9): 1065 (2017)

[26] Knorovsky G A, Cieslak M J, Headley T J, Romig A D, Hammetter W F. INCONEL 718: A solidification diagram. *Metall Trans A* **20**(10): 2149–2158 (1989)

[27] Burnett P J, Rickerby D S. The relationship between hardness and scratch adhesion. *Thin Solid Films* **154**(1–2): 403–416 (1987)

[28] Zhang D Y, Niu W, Cao X Y, Liu Z. Effect of standard heat treatment on the microstructure and mechanical properties of selective laser melting manufactured Inconel 718 superalloy. *Mater Sci Eng: A* **644**: 32–40 (2015)

[29] Munagala V N V, Torgerson T B, Scharf T W, Chromik R R. High temperature friction and wear behavior of cold-sprayed Ti6Al4V and Ti6Al4V-TiC composite coatings. *Wear* **426–427**: 357–369 (2019)

[30] Novak R, Polcar T. Tribological analysis of thin films by pin-on-disc: Evaluation of friction and wear measurement uncertainty. *Tribol Int* **74**: 154–163 (2014)

[31] De Baets P, Strijckmans K, Van Peteghem A P. A comparative study of different wear measurement techniques applied to fretting wear of a spherical against a flat steel specimen. *Tribotest* **4**(2): 129–143 (1997)

[32] Huang C M, Zou B, Liu Y N, Zhang S, Huang C Z, Li S S. Study on friction characterization and wear-resistance properties of Si_3N_4 ceramic sliding against different high-temperature alloys. *Ceram Int* **42**(15): 17210–17221 (2016)

[33] Stott F H, Wood G C. The influence of oxides on the friction and wear of alloys. *Tribol Int* **11**(4): 211–218 (1978)

[34] Qu S G, Lai F Q, Wang G H, Yuan Z M, Li X Q, Guo H. Friction and wear behavior of 30CrMnSiA steel at elevated temperatures. *J Mater Eng Perform* **25**(4): 1407–1415 (2016)

[35] Qiu M, Zhang Y Z, Zhu J, Luo X. The effect of dynamic frictional heating on the dry sliding behaviors of M2 steel against GCr15 steel. *Wear* **261**(7–8): 767–772 (2006)

[36] Vasudev H, Thakur L, Bansal A, Singh H, Zafar S. High temperature oxidation and erosion behaviour of HVOF sprayed bi-layer Alloy-718/NiCrAlY coating. *Surf Coat Technol* **362**: 366–380 (2019)

[37] Merz R, Brodyanski A, Kopnarski M. On the role of oxidation in tribological contacts under environmental conditions. *Conf Papers Sci* **2015**: 515498 (2015)

[38] Berlin J. Analysis of boron with energy dispersive X-ray spectrometry: Advances in light element analysis with SDD technology. *Imaging Microsc* 20–21 (2011)

[39] Mutalib M A, Rahman M A, Othman M H D, Ismail A F, Jaafar J. Chapter 9-Scanning Electron Microscopy (SEM) and Energy-Dispersive X-Ray (EDX) spectroscopy. In *Membrane Characterization*. Hilal N, Ismail A F, Matsuura T, Oatley-Radcliffe D, Eds. Amsterdam: Elsevier, 2017: 161–179.

[40] Lohaus C, Steinert C, Brötz J, Klein A, Jaegermann W. Systematic investigation of the electronic structure of hematite thin films. *Adv Mater Interfaces* **4**: 1700542 (2017)

[41] Dhoble S M, Kulkarni N S. Biosynthesis and characterization of different metal nanoparticles by using fungi. *Sch Acad J Biosci* **4**(11): 1022–1031 (2016)

[42] Phadungdhitidhada S, Mangkorntong P, Choopun S, Mangkorntong N. Raman scattering and electrical conductivity of nitrogen implanted MoO_3 whiskers. *Ceram Int* **34**(4): 1121–1125 (2008)

[43] Hong H S. The role of atmospheres and lubricants in the oxidational wear of metals. *Tribol Int* **35**(11): 725–729 (2002)

[44] Cai Z X, Li F M, Rong M C, Lin L P, Yao Q H, Huang Y P, Chen X, Wang X R. Chapter 1-Introduction. In *Novel Nanomaterials for Biomedical, Environmental and Energy Applications*. Wang X R, Chen X, Eds. Amsterdam: Elsevier, 2019: 1–36.

[45] Torres H, Ripoll M R, Prakash B. Tribological behaviour of self-lubricating materials at high temperatures. *Int Mater Rev* **63**(5): 309–340 (2018)

[46] Chen F Y, Feng Y, Shao H, Zhang X B, Chen J, Chen N N. Friction and wear behaviors of $Ag/MoS_2/G$ composite in different atmospheres and at different temperatures. *Tribol Lett* **47**(1): 139–148 (2012)

[47] Hamdani F. Improvement of the corrosion and oxidation resistance of Ni-based alloys by optimizing the chromium content. Ph.D Thesis. Senda (Japan): Tohoku Gakuin

University, 2015.

[48] Tuzi S. Electron microscopy of oxide formed on nickel alloy X-750 in simulated boiling water reactor environment. Ph.D Thesis. Goteborg (Sweden): Chalmers University of Technology, 2017.

[49] Radhakrishnan R, Oyama S T, Chen J G, Asakura K. Electron transfer effects in ozone decomposition on supported manganese oxide. *J Phys Chem B* **105**(19): 4245–4253 (2001)

[50] Mougin J, Le Bihan T, Lucazeau G. High-pressure study of Cr_2O_3 obtained by high-temperature oxidation by X-ray diffraction and Raman spectroscopy. *J Phys Chem Solids* **62**(3): 553–563 (2001)

[51] Trindade V, Krupp U, Wagenhuber E G, Christ H J. Oxidation mechanisms of Cr-containing steels and Ni-base alloys at high-temperatures–Part I: The different role of alloy grain boundaries. *Mater Corros* **56**(11): 785–790 (2005)

[52] Ichimura H, Kawana A. High temperature oxidation of ion-plated CrN films. *J Mater Res* **9**(1): 151–155 (1994)

[53] Li R, He D Y, Zhou Z, Wang Z J, Song X Y. Wear and high temperature oxidation behaviour of wire arc sprayed iron based coatings. *Surface Eng* **30**(11): 784–790 (2014)

[54] Yilmaz C, Unal U. Effect of cerium doping on morphology and physical properties of α-Fe_2O_3 films prepared by hydrothermal electrodeposition. *ECS Trans* **58**(19): 55–63 (2014)

[55] Shui Y, Feng K Q, Zhang Y Y, Yan Z D. Influence of Mn on the iron-based friction material directly prepared by *in situ* carbothermic reaction from vanadium-bearing titanomagnetite concentrates. *RSC Adv* **8**(64): 36503–36511 (2018)

[56] Salvaro D B, Silvério M, Binder C, Giacomelli R O, Klein A N, De Mello J D B. Genesis and stability of tribolayers in solid lubrication: Case of pair DLC-stainless steel. *J Mater Res Technol* **5**(2): 136–143 (2016)

[57] Eyre T S. Wear characteristics of metals. *Tribol Int* **9**(5): 203–212 (1976)

[58] Hardell J, Hernandez S, Mozgovoy S, Pelcastre L, Courbon C, Prakash B. Effect of oxide layers and near surface transformations on friction and wear during tool steel and boron steel interaction at high temperatures. *Wear* **330–331**: 223–229 (2015)

[59] Yun J Y, Park D, Wang J P. A study on the oxidation behavior of nickel alloys at elevated temperatures. *IOP Conf Series Mater Sci Eng* **191**(1): 012039 (2017)

[60] Wahl K J, Seitzman L E, Bolster R N, Singer I L, Peterson M B. Ion-beam deposited Cu-Mo coatings as high temperature solid lubricants. *Surface Coat Technol* **89**(3): 245–251 (1997)

[61] Holcomb G R, Tylczak J, Carney C. Oxidation of CoCrFeMnNi high entropy alloys. *JOM* **67**(10): 2326–2339 (2015)

[62] Quinn T F J. Review of oxidational wear: Part I: The origins of oxidational wear. *Tribol Int* **16**(5): 257–271 (1983)

[63] Quinn T F J. Review of oxidational wear part II: Recent developments and future trends in oxidational wear research. *Tribol Int* **16**(6): 305–315 (1983)

[64] Singer I L. Solid lubricating films for extreme environments. *MRS Online Proc Libr Arch* **140**: 215 (1988)

[65] Lancaster J K. The formation of surface films at the transition between mild and severe metallic wear. *Proc Royal Soc London Series A. Math Phys Sci* **273** (1355): 466–483 (1963)

[66] Pauschitz A, Roy M, Franek F. Mechanisms of sliding wear of metals and alloys at elevated temperatures. *Tribol Int* **41**(7): 584–602 (2008)

[67] Stott F H, Lin D S, Wood G C. The structure and mechanism of formation of the 'glaze' oxide layers produced on nickel-based alloys during wear at high temperatures. *Corros Sci* **13**(6): 455–469 (1973)

[68] Stott F H. The role of oxidation in the wear of alloys. *Tribol Int* **31**(1–3): 61–71 (1998)

[69] Vashishtha N, Sapate S G. Abrasive wear maps for High Velocity Oxy Fuel (HVOF) sprayed WC-12Co and Cr_3C_2−25NiCr coatings. *Tribol Int* **114**: 290–305 (2017)

[70] Vashishtha N, Sapate S G, Gahlot J S, Bagde P. Effect of tribo-oxidation on friction and wear behaviour of HVOF sprayed WC–10Co–4Cr coating. *Tribol Lett* **66**(2): 56 (2018)

[71] Trevisiol C, Jourani A, Bouvier S. Effect of hardness, microstructure, normal load and abrasive size on friction and on wear behaviour of 35NCD16 steel. *Wear* **388–389**: 101–111 (2017)

[72] Bhatt A, Attia H, Vargas R, Thomson V. Wear mechanisms of WC coated and uncoated tools in finish turning of Inconel 718. *Tribol Int* **43**(5–6): 1113–1121 (2010)

[73] Dorner-Reisel A, Schürer C, Müller E. The wear resistance of diamond-like carbon coated and uncoated Co28Cr6Mo knee prostheses. *Diam Relat Mater* **13**(4–8): 823–827 (2004)

Liuyang BAI. He obtained his bachelor degree in School of Material Sciences and Engineering in 2018 from North Minzu University, Yinchuan, China. Currently he is a M.S. student at the Lanzhou Institute of Chemical Physics, China. His current research is the tribological system of the metal/ceramic and ceramic/ceramic.

Shanhong WAN. He received his Ph.D. degree in the State Key Laboratory of Solid Lubrication at Lanzhou Institute of Chemical Physics, Chinese Academy of Sciences, China, in 2010. His current position is a professor. His research areas cover high-temperature tribology of metal-ceramic composites and associated tribochemistry, and surface engineering.

Gewen YI. He received his Ph.D. degree in the State Key Laboratory of Solid Lubrication at Lanzhou Institute of Chemical Physics, Chinese Academy of Sciences, China, in 2007. His research focuses on tribological dynamics and microstructure characterization of solid lubricants subjected to a broad temperature range.